energies

MDPI

Article

Analysis on Filling Ratio and Shield Supporting Pressure for Overburden Movement Control in Coal Mining with Compacted Backfilling

Yanli Huang, Junmeng Li *, Tianqi Song, Guoqiang Kong and Meng Li

State Key Laboratory of Coal Resources and Safe Mining, School of Mines,
China University of Mining & Technology, Xuzhou 221116, China; huangyanli6567@163.com (Y.H.);
stq344359844@163.com (T.S.); kgq9569913@163.com (G.K.); 1119569913@qq.com (M.L.)
* Correspondence: lijunmeng1201@163.com; Tel.: +86-1505-0836-128

Academic Editor: Vasily Novozhilov
Received: 13 November 2016; Accepted: 22 December 2016; Published: 30 December 2016

Abstract: Since the weight of overburden is sustained by both the backfill body and the unmined solid coal in coal mining with compacted backfilling (CMCB) panels, the stress and deformation characteristics of the surrounding rocks in coal mining are radically changed. The overburden movement control mechanism by coordinating with backfill body and shield in CMCB was studied systematically in this paper. Based on the analysis of deformational and structural characteristics of surrounding rock in CMCB panels, the methods of theoretical analysis, numerical simulation and engineering test are employed. The results show that the fracture of the main roof is mainly controlled by the filling ratio φ and is non-correlated to the shield supporting pressure p. However, p has a significant control effect on the deflection of roof within the shield canopy length, and adversely affects the filling ratio. With the increase of the filling ratio of the gob, the maximum sagging of the immediate and the main roofs, the peak front and the influence range of the abutment pressures are gradually reduced. Correspondingly, the stable period of internal pressure of backfill body in the gob is shortened. Engineering practice shows that the sagging of the gob roof, the distribution of the abutment pressure, the distribution of the internal pressure in the backfill body, and the ground surface sagging results obtained by the in-situ measurement are approximately corresponding to the theoretical analysis and numerical simulation results.

Keywords: coal mining with compacted backfilling (CMCB); filling ratio; shield supporting pressure; overburden movement; elastic-thin-plate mechanical model; numerical simulation

1. Introduction

With the development of mining technology, several methods of refilling or backfilling the developed voids, such as the hydraulic backfill, cemented paste backfill, rock backfill and silica alumina-based backill methods have been proposed [1]. Hydraulic backfill uses water as the transportation medium to convey the hydraulic backfill materials, such as waste tailings, water hydrophilic slag, mountain sand, river sand, and crushing sand to fill underground mined voids like stopes [2]. Hydraulic backfill can be placed cemented or non-cemented, of which the latter one is one of the cheapest methods in mines when small size waste particles are available [3]. Cemented paste backfill (CPB) is a non-homogenous material made by mixing waste tailings, water, and cement. CPB is one of new and fast growing waste management and backfill technologies used in the mining industry, which creates an economical way of providing support and safe working place in underground mining development beside its environmental benefits [4,5]. Rock backfill can be described as a technology for transportation of backfill forming components such as stone, gravel, soil, industrial solid waste

using manpower, gravity or machinery equipment to fill underground mined voids and production of compressed backfill body. This method decreases waste material on the surface and expands usable land on the ground, decreases environmental pollution by transferring waste rocks to deeper levels out of rain contact, increases stability of mined area and decreases land subsidence and rock bursts due to stress pattern changes [6].

Coal mining with compacted backfilling (CMCB) technology is a "green mining" technology, which is proposed for the problems of coal seams under structures, under underground aquifers and under infrastructures (3U coal seam), and solvents of the gangue in coal mining [7,8]. Solid wastes, such as gangue, aeolian sand and open pit mine slags are backfilled into the gob. Simultaneously, the purpose of replacing the 3U coal seam, controlling the overburden movement, and protection of surface buildings are achieved [9,10]. In CMCB panels, the backfill body serves as a supporting structure and sustains most of the load from the overburden above the gob. It changes the characteristics of stress redistribution in surrounding rock, and restricts the crack widely development and large area caving of roof. Different from the traditional coal caving mining method, the weight of overburden is carried by both the backfill body and the unmined solid coal in CMCB, and the stress distribution and deformation characteristics of surrounding rocks in coal mining are changed radically [11–13].

To date, most theoretical studies have focused on the characters and features of overburden movement in CMCB. The equivalent mining height theory of backfill mining [7] was proposed for the key stratum foundation beam theory [14] and the elastic foundation beam of the roof theory [15], etc. In CMCB, the backfilling degree of the gob can be measured by the filling ratio, which is the value of the final height of the compacted backfill body to the mining height [16]. These studies provided useful guidance in understanding the deformational characteristics of overburden at the middle of the panel, but still have their limits. Therefore, an elastic-thin-plate mechanical model is not only established, but also solved in this paper. Meanwhile, overburden movement control mechanism by coordination with backfill body and shield in CMCB were also studied systematically by using numerical simulations. Thereafter, the results of the elastic-thin-plate mechanical model derivation are verified by an engineering practice. The conclusions could serve as reference and guidance for further study on the theory of the overburden movement in CMCB.

2. Comparison of Overburden Deformational Characteristics between Traditional Caving Method and Coal Mining with Compacted Backfilling (CMCB) Method

2.1. Overburden Deformational Characteristics in Traditional Caving Method

In the traditional caving method, periodic fracturing and caving of the immediate and the main roofs were observed with the advancement of the working face. When the gob area was large enough, the resulted disturbance due to the underground excavation may reach the ground surface, creating a surface sagging basin whose area was greater than the gob area. The overburden can be divided into "three horizontal zones" and "three vertical zones" based on their movement and failure characteristics: the coal wall abutment pressure affecting zone, the separation zone and the recompaction zone in horizontal direction; and the caving zone, the fractured zone and the continuous deformation zone in the vertical direction. Figure 1 shows a diagram of the spatial relationship of the "three horizontal zones" and the "three vertical zones" [17].

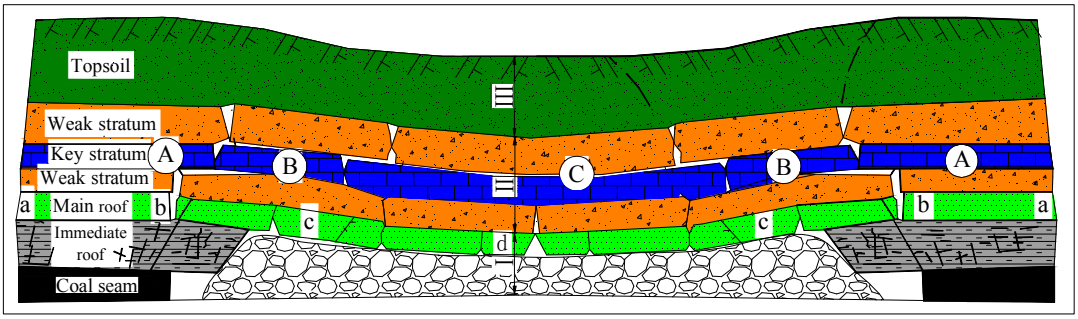

Figure 1. The "three horizontal zones" and "three vertical zones" of overburden strata movement (Qian et al, 2003 [17]). A—abutment pressure affecting area (a–b); B—separation area (b–c); C—recompaction area (c–d); I—caving zone; II—fracture zone; III—bending sagging zone.

2.2. Overburden Deformation Characteristics in Coal Mining with Compacted Backfilling (CMCB) Method

In CMCB panels, backfill body such as gangue was timely filled into the gob. After compacting by the compactor of the shield [9], the backfill body would have full contact with the roof, thus, it can be seen as a supporting structure. Once in place, it will sustain the load of overburden above the gob, and further, restrict the sagging of the immediate and the main roofs, and prevent them from fracturing and caving. The overburden movement is featured by bending, deflection and local fractures, without caving zone. Consequently, the deformation behaviors of surrounding rocks were totally changed [18], as seen in Figure 2.

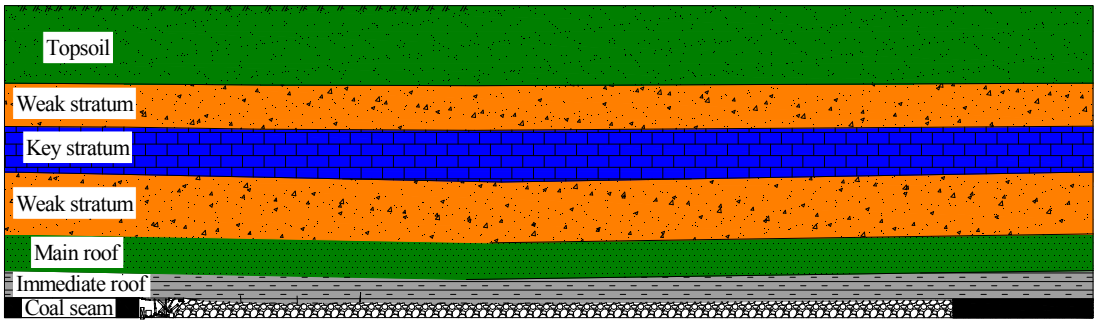

Figure 2. Features of overburden strata movement in coal mining with compacted backfilling (CMCB) method [11].

3. Establishment and Solving of Elastic-Thin-Plate Mechanical Model of Overburden in CMCB

3.1. Establishment of Elastic-Thin-Plate Mechanical Model of Overburden Strata Movement in CMCB

According to the Winkler hypothesis [19], if a plate were placed on a continuous elastic foundation and bent under the load [$q(x,y)$] perpendicular to the plate, the contact pressure, R, is proportional to the deflection, w, given the condition that the deflection is far smaller than the thickness of the plate:

$$R = kw \tag{1}$$

where k refers to the elastic foundation coefficient. The load on a point on the plate, Q, can be calculated as follows:

$$Q = q(x,y) - kw \tag{2}$$

The deflection of the elastic foundation would be consistent with the following differential equation:

$$D\left(\frac{\partial^4 w}{\partial x^4} + 2\frac{\partial^4 w}{\partial x^2 \partial y^2} + \frac{\partial^4 w}{\partial y^4}\right) = q(x,y) - kw \tag{3}$$

where D refers to the flexural rigidity of the plate, $D = \frac{Eh^3}{12(1-v^2)}$; E refers to the elastic modulus of the plate; v refers to Poisson ratio; h refers to thickness of the plate.

In CMCB, the typical length of panel, l, was around 100–150 m, the advancement length, L, was around 1000–2000 m, and the thickness, h, of the main roof was about 3–20 m. Thus the value of h/l can be estimated to be between 1/50 and 1/5. According to the theory of elastic-thin-plate [20,21], the main roof can be categorized as an elastic-thin-plate.

The main roof thus was regarded as an elastic-thin-plate with fixed boundary conditions at the four edges of the plate. The loads on the elastic-thin-plate, q, which is a load from the overburden, is assumed to be uniformly distributed. The working pressure of the shield on the main roof could be simplified as a uniform pressure, p. The immediate roof and backfill body can be seen as an elastic foundation. The pressure delivered to the main roof from this elastic foundation is related to the deflection of the main roof and can be calculated using Equation (1). The final simplified model for the main roof in CMCB is illustrated in Figure 3.

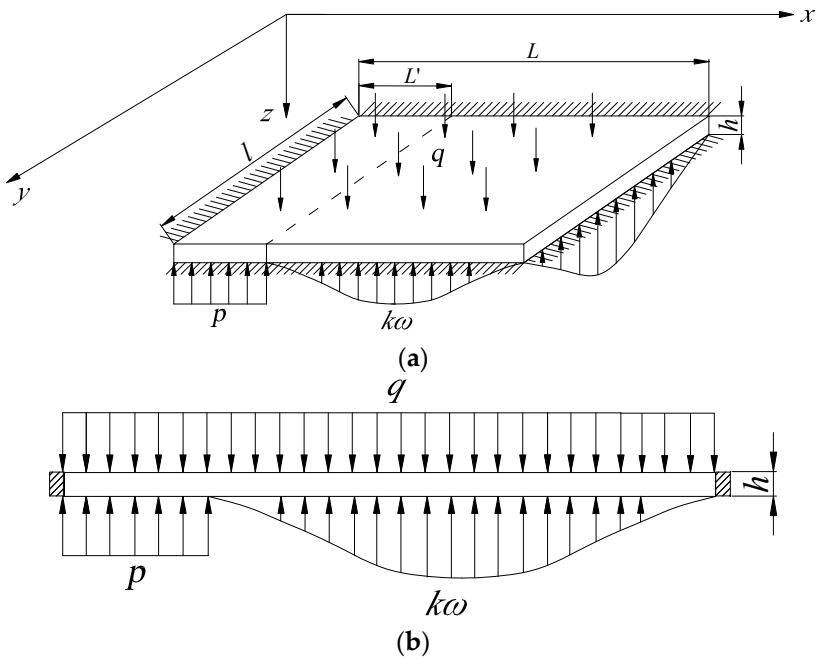

Figure 3. Elastic-thin-plate mechanical model of main roof in CMCB. (**a**) 3-D view of model; (**b**) Section view of model.

The establishment of the coordinate system is as shown in Figure 4. Here, l refers to the length of panel, L refers to the advancement length of the panel, L' refers to the shield length, q refers to the uniform load of overburden on the main roof, p refers to the supporting pressure of the shield, k refers to the elastic foundation coefficient and ω refers to the deflection of main roof.

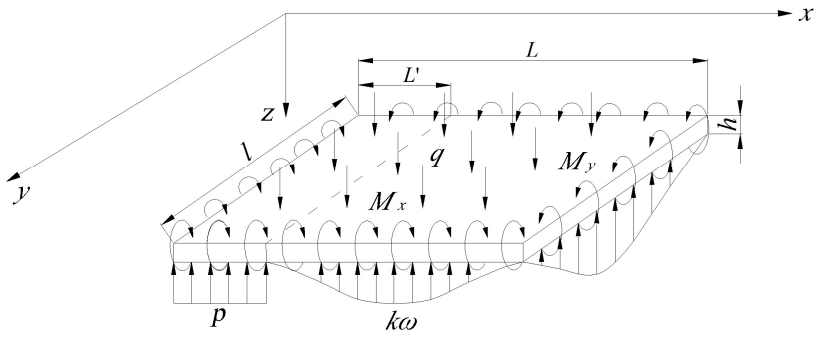

Figure 4. Simplified elastic-thin-plate mechanical model of main roof.

Based on the principle of equivalent substitution [22], the fixed boundary conditions at the four edges of the proposed model can be replaced by the hinged boundary with an unknown distribution of bending moment $M(x)|_{\substack{y=0\\y=l}}$ and $M(y)|_{\substack{x=0\\x=L}}$, which act on those boundaries if the deformation character at those boundaries would maintain. Bending moment $M(x)|_{\substack{y=0\\y=l}}$ distribution in both $y = 0$, $y = l$ sides changes with the x location of each point. Bending moment $M(y)|_{\substack{x=0\\x=L}}$ distribution in both $x = 0$, $x = l$ sides changes with the y location of each point. For fixed boundary condition, the deflection and the first derivative of the deflection at the direction normal to the boundary would be zero, as shown in Equation (4):

$$\begin{cases} (w)_{\substack{x=0\\x=L}} = 0 \\ (\dfrac{\partial w}{\partial x})_{\substack{x=0\\x=L}} = 0 \\ (w)_{\substack{y=0\\y=l}} = 0 \\ (\dfrac{\partial w}{\partial y})_{\substack{y=0\\y=l}} = 0 \end{cases} \tag{4}$$

These conditions will stay true in the equivalent model.

The simplified mechanical model after the equivalent substitution is also shown in Figure 4.

3.2. Solving of the Elastic-Thin-Plate Model

According to the simplified elastic-thin-plate mechanical model, the double sine series selected by Navier [23,24] was used to express the deflection equation of the plate:

$$w = \sum_{m=1,3\ldots}^{\infty} \sum_{n=1,3\ldots}^{\infty} a_{mn} \sin \frac{m\pi x}{L} \sin \frac{n\pi y}{l} \tag{5}$$

Here, the coefficient a_{mn} could be calculated by the principle of virtual displacement [25]. The first derivative of deflection along $y = 0$, $y = l$ and $x = 0$, $x = L$ was calculated as follows:

$$\begin{cases} (\dfrac{\partial w}{\partial y})_{\substack{y=0\\y=l}} = \pm \dfrac{\pi}{l} \sum\limits_{m=1,3\ldots}^{\infty} \sum\limits_{n=1,3\ldots}^{\infty} n a_{mn} \sin \dfrac{m\pi x}{L} \\ (\dfrac{\partial w}{\partial x})_{\substack{x=0\\x=L}} = \pm \dfrac{\pi}{L} \sum\limits_{m=1,3\ldots}^{\infty} \sum\limits_{n=1,3\ldots}^{\infty} m a_{mn} \sin \dfrac{n\pi y}{l} \end{cases} \tag{6}$$

The main roof, shield, and elastic foundation were considered as an integrated system. Using the principle of virtual displacement, the sum of the work done by the uniform load of the overburden, the moment acting on the hinged boundaries on the virtual displacement, and the increment of deformation energy of the entire system equals to zero.

Here, the bending deformation energy dV_1 at a point in the plate was calculated as follows:

$$dV_1 = -\frac{1}{2}[M_x\frac{\partial^2 w}{\partial x^2} + M_y\frac{\partial^2 w}{\partial y^2} + 2M_{xy}\frac{\partial^2 w}{\partial x \partial y}]dxdy \tag{7}$$

where M_x, M_y, M_{xy} refer to bending moments, which can be expressed as follows.

$$\begin{cases} M_x = -D(\frac{\partial^2 w}{\partial x^2} + \mu\frac{\partial^2 w}{\partial y^2}) \\ M_y = -D(\frac{\partial^2 w}{\partial y^2} + \mu\frac{\partial^2 w}{\partial x^2}) \\ M_{xy} = -D(1-\mu)\frac{\partial^2 w}{\partial x \partial y} \end{cases}$$

Integrate Equation (7) for x and y:

$$V_1 = \frac{1}{2}D\int\int\{(\frac{\partial^2 w}{\partial x^2} + \frac{\partial^2 w}{\partial y^2})^2 - 2(1-\mu)[\frac{\partial^2 w}{\partial x^2}\frac{\partial^2 w}{\partial y^2} - (\frac{\partial^2 w}{\partial x \partial y})^2]\}dxdy \tag{8}$$

The deformation energy, V_1, of the plate can be calculated by Equation (9).

$$V_1 = \frac{\pi^4 LlD}{8}\sum_{m=1,3\ldots}^{\infty}\sum_{n=1,3\ldots}^{\infty} a_{mn}^2(\frac{m^2}{L^2} + \frac{n^2}{l^2})^2 \tag{9}$$

The deformation energy, V_2, of the elastic foundation can be calculated by Equation (10).

$$V_2 = \int_0^l\int_{L\prime}^{L}\frac{kw^2}{2}dxdy = \sum_{m=1,3\ldots}^{\infty}\sum_{n=1,3\ldots}^{\infty}\frac{ka_{mn}^2}{16}[2l(L-L') - \frac{Ll}{m\pi}\sin\frac{2m\pi L'}{L}] \tag{10}$$

The deformation energy, V_3, of the shield can be calculated by Equation (11).

$$V_3 = \int_0^l\int_0^{L'}\frac{Pw}{2}dxdy = \sum_{m=1,3\ldots}^{\infty}\sum_{n=1,3\ldots}^{\infty}\frac{Pa_{mn}Ll}{mn\pi^2}(1-\cos\frac{mL'\pi}{L}) \tag{11}$$

The total deformation energy of the system can be calculated by

$$V = V_1 + V_2 + V_3$$

when $a_{mn}V$ was increased by δa_{mn}, the increment of the deformation energy of the system was calculated as follows:

$$\begin{aligned}\delta V = {} & \frac{Ll\pi^4}{4}D\sum_{m=1,3\ldots}^{\infty}\sum_{n=1,3\ldots}^{\infty}a_{mn}(\frac{m^2}{L^2} + \frac{n^2}{l^2})^2\delta a_{mn} + \sum_{m=1,3\ldots}^{\infty}\sum_{n=1,3\ldots}^{\infty}[\frac{ka_{mn}l(L-L')\delta a_{mn}}{4} \\ & + \frac{PLl\delta a_{mn}}{mn\pi^2}] - \sum_{m=1,3\ldots}^{\infty}\sum_{n=1,3\ldots}^{\infty}(\frac{ka_{mn}Ll\delta a_{mn}}{8m\pi}\sin\frac{2m\pi L'}{L} + \frac{PLl\delta a_{mn}}{mn\pi^2}\cos\frac{mL'\pi}{L})\end{aligned} \tag{12}$$

The virtual work, δT, done by the uniform load q of overburden, and the bending moments $M(x)\Big|_{\substack{y=0\\y=l}}$ and $M(y)\Big|_{\substack{x=0\\x=L}}$ on the hinged boundary can be expressed as follows.

$$\begin{aligned}\delta T &= \int_0^L\int_0^l q\delta w dxdy + 2\int_0^L M(x)\Big|_{\substack{y=0\\y=l}} dx\delta(\frac{\partial w}{\partial y})_{y=0} + 2\int_0^l M(y)\Big|_{\substack{x=0\\x=L}} dy\delta(\frac{\partial w}{\partial x})_{x=0}\\ &= \int_0^L\int_0^l q\delta a_{mn}\sin\frac{m\pi x}{L}\sin\frac{n\pi y}{l}dxdy + 2\frac{n\pi}{l}\int_0^L M(x)\Big|_{\substack{y=0\\y=l}} dx\sin\frac{m\pi x}{L}\delta a_{mn}\\ &+2\frac{m\pi}{L}\int_0^l M(y)\Big|_{\substack{x=0\\x=L}} dy\sin\frac{n\pi y}{l}\delta a_{mn} = [\frac{4Llq}{mn\pi^2} + \frac{n\pi}{l}LE_m + \frac{m\pi}{L}lF_n]\delta a_{mn}\end{aligned} \tag{13}$$

In Equation (13), E_m and F_n refer to the coefficients in terms of that $M(x)\Big|_{\substack{y=0\\y=l}}$ and $M(y)\Big|_{\substack{x=0\\x=L}}$ were expanded into a Fourier series [26]:

$$\begin{cases} M(x)\Big|_{\substack{y=0\\y=l}} = \sum\limits_{m=1,3\ldots}^{\infty} E_m\sin\dfrac{m\pi x}{L}\\ M(y)\Big|_{\substack{x=0\\x=L}} = \sum\limits_{n=1,3\ldots}^{\infty} F_n\sin\dfrac{n\pi y}{l}\end{cases} \tag{14}$$

According to the virtual displacement principle and by reorganizing equation, the expression for a_{mn} could be obtained:

$$a_{mn} = \frac{\frac{Ll}{mn\pi^2}\left(4q - p + p\cos\frac{mL'\pi}{L}\right) + \frac{n\pi}{l}LE_m + \frac{m\pi}{L}lF_n}{\frac{Ll\pi^4}{4}D(\frac{m^2}{L^2}+\frac{n^2}{l^2})^2 + \frac{kl(L-L')}{4} - \frac{kLl}{8m\pi}\sin\frac{2m\pi L'}{L}} \tag{15}$$

After substituting Equation (15) into Equation (5), the expression for the deflection becomes:

$$\begin{aligned}w = \sum_{m=1,3\ldots}^{\infty}\sum_{n=1,3\ldots}^{\infty} &\frac{1}{\frac{Ll\pi^4}{4}D(\frac{m^2}{L^2}+\frac{n^2}{l^2})^2 + \frac{kl(L-L')}{4} - \frac{kLl}{8m\pi}\sin\frac{2m\pi L'}{L}}[\frac{Ll}{mn\pi^2}\\ &\left(4q - p + p\cos\frac{mL'\pi}{L}\right) + \frac{n\pi}{l}LE_m + \frac{m\pi}{L}lF_n]\sin\frac{m\pi x}{L}\sin\frac{n\pi y}{l}\end{aligned} \tag{16}$$

Partially differentiate Equation (16) by y and by x, the partial derivative of deflection on boundary $x = 0$ and $y = 0$ can be expressed by Equation (17):

$$\begin{cases} (\dfrac{\partial w}{\partial y})_{y=0} = \dfrac{\pi}{l}\displaystyle\sum_{m=1,3\ldots}^{\infty}\sum_{n=1,3\ldots}^{\infty} \dfrac{1}{\frac{Ll\pi^4}{4}D(\frac{m^2}{L^2}+\frac{n^2}{l^2})^2 + \frac{kl(L-L')}{4} - \frac{kLl}{8m\pi}\sin\frac{2m\pi L'}{L}}[\\ \dfrac{Ll}{m\pi^2}\left(4q - p + p\cos\dfrac{mL'\pi}{L}\right) + \dfrac{n^2\pi}{l}LE_m + \dfrac{mn\pi}{L}lF_n]\sin\dfrac{m\pi x}{L}\\ (\dfrac{\partial w}{\partial x})_{x=0} = \dfrac{\pi}{L}\displaystyle\sum_{m=1,3\ldots}^{\infty}\sum_{n=1,3\ldots}^{\infty} \dfrac{1}{\frac{Ll\pi^4}{4}D(\frac{m^2}{L^2}+\frac{n^2}{l^2})^2 + \frac{kl(L-L')}{4} - \frac{kLl}{8m\pi}\sin\frac{2m\pi L'}{L}}[\\ \dfrac{Ll}{n\pi^2}\left(4q - p + p\cos\dfrac{mL'\pi}{L}\right) + \dfrac{mn\pi}{l}LE_m + \dfrac{m^2\pi}{L}lF_n]\sin\dfrac{n\pi y}{l}\end{cases} \tag{17}$$

Since the conditions shown in Equation (4) would be maintained in the simplified model:

$$\begin{cases} \left(\frac{\partial w}{\partial x}\right)_{\substack{x=0 \\ x=L}} = 0 \\ \left(\frac{\partial w}{\partial y}\right)_{\substack{y=0 \\ y=l}} = 0 \end{cases} \tag{18}$$

Equating the right hand side of Equation (17) with zero and getting:

$$\begin{cases} \sum\limits_{n=1,3\ldots}^{\infty}\sum\limits_{m=1,3\ldots}^{\infty} \dfrac{1}{\frac{Ll\pi^4}{4}D\left(\frac{m^2}{L^2}+\frac{n^2}{l^2}\right)^2+\frac{kl(L-L')}{4}-\frac{kLl}{8m\pi}\sin\frac{2m\pi L'}{L}} \\ \left[\frac{Ll}{m\pi^2}\left(4q-p+p\cos\frac{mL'\pi}{L}\right)+\frac{n^2\pi}{l}LE_m+\frac{mn\pi}{L}lF_n\right]=0 \\ \sum\limits_{m=1,3\ldots}^{\infty}\sum\limits_{n=1,3\ldots}^{\infty} \dfrac{1}{\frac{Ll\pi^4}{4}D\left(\frac{m^2}{L^2}+\frac{n^2}{l^2}\right)^2+\frac{kl(L-L')}{4}-\frac{kLl}{8m\pi}\sin\frac{2m\pi L'}{L}} \\ \left[\frac{Ll}{n\pi^2}\left(4q-p+p\cos\frac{mL'\pi}{L}\right)+\frac{mn\pi}{l}LE_m+\frac{m^2\pi}{L}lF_n\right]=0 \end{cases} \tag{19}$$

In Equation (19), the Fourier coefficients E_1, E_3, E_5, E_7, ... and F_1, F_3, F_5, F_7, ... could be solved through the successive approximation method.

The relationship between the mining height, the filling ratio and the final sagging of the roof can be described by Equation (20):

$$\varphi = \frac{h-\Delta}{h} \tag{20}$$

where h refers to the mining height, φ refers to the filling ratio, and Δ refers to the final sagging of roof.

The relationship between the elastic foundation coefficient and the final sagging of the roof is shown as follows:

$$\Delta = \frac{\sigma_0}{k} \tag{21}$$

where σ_0 refers to in-situ stress, and k refers to the elastic foundation coefficient.

The relationship between the elastic foundation coefficient and filling ratio, φ, was then deduced from Equations (20) and (21):

$$k = \frac{\sigma_0}{h(1-\varphi)} \tag{22}$$

In a certain geological condition, σ_0 and h are constant, thus, the elastic foundation coefficient is mainly related to the filling ratio of the gob in CMCB.

Substitute k in Equation (16) with the expression in Equation (22), the deflection of the plate can now be expressed as follows:

$$w = \sum_{m=1,3\ldots}^{\infty}\sum_{n=1,3\ldots}^{\infty} \frac{1}{\frac{Ll\pi^4}{4}D\left(\frac{m^2}{L^2}+\frac{n^2}{l^2}\right)^2+\frac{\sigma_0 l(L-L')}{4h(1-\varphi)}-\frac{\sigma_0 Ll}{8m\pi h(1-\varphi)}\sin\frac{2m\pi L'}{L}}\left[\frac{Ll}{mn\pi^2}\left(4q-p+p\cos\frac{mL'\pi}{L}\right)+\frac{n\pi}{l}LE_m+\frac{m\pi}{L}lF_n\right]\sin\frac{m\pi x}{L}\sin\frac{n\pi y}{l} \tag{23}$$

From Equation (23), the expression of the bending moments on the plate, M_x and M_y, can be derived:

$$M_x = -4D\pi^2\left(\frac{m^2}{L^2}+\mu\frac{n^2}{l^2}\right)\sum_{m=1,3\ldots}^{\infty}\sum_{n=1,3\ldots}^{\infty}\frac{1}{Ll\pi^4 D\left(\frac{m^2}{L^2}+\frac{n^2}{l^2}\right)^2+\frac{\sigma_0 l(L-L')}{h(1-\varphi)}-\frac{\sigma_0 Ll}{2m\pi h(1-\varphi)}\sin\frac{2m\pi L'}{L}} \left[\frac{Ll}{mn\pi^2}\left(4q-p+p\cos\frac{mL'\pi}{L}\right)+\frac{n\pi}{l}LE_m+\frac{m\pi}{L}lE_m+\frac{m\pi}{L}lF_n\right]\sin\frac{m\pi x}{L}\sin\frac{n\pi y}{l} \tag{24}$$

$$M_y = -4D\pi^2\left(\mu\frac{m^2}{L^2}+\frac{n^2}{l^2}\right)\sum_{m=1,3\ldots}^{\infty}\sum_{n=1,3\ldots}^{\infty}\frac{1}{Ll\pi^4 D\left(\frac{m^2}{L^2}+\frac{n^2}{l^2}\right)^2+\frac{\sigma_0 l(L-L')}{h(1-\varphi)}-\frac{\sigma_0 Ll}{2m\pi h(1-\varphi)}\sin\frac{2m\pi L'}{L}} \left[\frac{Ll}{mn\pi^2}\left(4q-p+p\cos\frac{mL'\pi}{L}\right)+\frac{n\pi}{l}LE_m+\frac{m\pi}{L}lE_m+\frac{m\pi}{L}lF_n\right]\sin\frac{m\pi x}{L}\sin\frac{n\pi y}{l} \tag{25}$$

3.3. Critical Conditions of Main Roof Failure

The maximum stress component within the plate:

$$\begin{cases} \sigma_{x,\max} = \dfrac{12M_{x,\max}z}{h^3} \\ \sigma_{y,\max} = \dfrac{12M_{y,\max}z}{h^3} \\ \tau_{xy,\max} = \dfrac{12M_{xy,\max}z}{h^3} \end{cases} \tag{26}$$

Through analysis of Equations (24) and (25), it was found that the maximum bending moment was on the fixed side. The bending moment can be expressed in Fourier series and the expression is shown in Equation (14) in previous sections.

$M_{x,\max}$ and $M_{y,\max}$ were replaced in Equation (26) with the expression, as shown in Equation (14). The expression for maximum tensile stress within the plate can thus be derived. The main roof would stay stable if the maximum tensile stress in the plate is less than the tensile strength of the main roof:

$$\begin{cases} \sigma_{x,\max} = \dfrac{6M(x)\Big|_{\substack{y=0\\y=l}}}{h^2} = \dfrac{6}{h^2}\sum\limits_{m=1,3\ldots}^{\infty}E_m\sin\dfrac{m\pi x}{L} \le [\sigma_t] \\ \sigma_{y,\max} = \dfrac{6M(y)\Big|_{\substack{x=0\\x=L}}}{h^2} = \dfrac{6}{h^2}\sum\limits_{n=1,3\ldots}^{\infty}F_n\sin\dfrac{n\pi y}{l} \le [\sigma_t] \end{cases} \tag{27}$$

3.4. Application of Analysis Result on an Actual Case

From the deflection and maximum tensile stress equations of the main roof in CMCB, the main factors influencing the deflection and maximum tensile stress of main roof include: filling ratio, φ, the length of the panel, l, the advancement length, L, the elastic modulus of the main roof, E, load of overburden above the main roof, q, and the working pressure of the shield, p. Under a certain mining geological condition l, L, h, E, q are approximately constant, so the filling ratio φ and the working pressure of the shield p are the most important factors influencing the movement of the roof.

In this section, we will analyze the cooperative roof control effect of the filling ratio and the working pressure of the shield in CMCB, using the field data from Panel 13080 of Pingdingshan No. 12 Coal Mine. In this field case, the length of the panel, l, was 100 m; the advancement length, L, was 350 m; the thickness of the coal seam was 3.3 m; the dip angle of the coal seam was found to be 0°–4°. The main roof was a sandstone layer with a thickness of 31.5 m. The elastic modulus

E of the sandstone was 28 GPa, and the Poisson's ratio ν was 0.25, while the uniform load q from the overburden was 4.0 MPa (the depth of cover between main roof and main key stratum, H, was 156.9 m, and the average unit weight γ of the overburden strata was 25 kN/m^3) [27,28], The shield canopy length L' was 8 m.

(1) Effect of filling ratio and working pressure of shield on main roof stability

The first two terms of the Fourier expansion were used to express the bending moments on the fixed boundaries, $M(x)\big|_{\substack{y=0\\y=l}}$ and $M(y)\big|_{\substack{x=0\\x=L}}$. The solving of E_1, E_3, F_1 and F_3 was done by the mathematical tool software, Maple. Replace the E_1, E_3, F_1 and F_3 in Equation (26) and get the expression for maximum tensile stress in the main roof, $\sigma_{t,\max}$, as a function of shield supporting pressure, p, and the filling ratio, φ:

$$\sigma_{t\max} = \frac{3.81\varphi \times 10^8 + 17.5p\varphi + 4.89 \times 10^9 + 0.746p}{414\varphi - 1025} \tag{28}$$

The relationship between the maximum tensile stress in the main roof and the shield supporting pressure and filling ratio drawn by the Maple software was shown in Figure 5.

As shown in Figure 5, when the filling ratio of the gob remains constant, increasing or decreasing the shield supporting pressure, p, will have little influence on the maximum tensile stress of the main roof. Therefore, the influence of the shield supporting pressure, p, on the maximum tensile stress of the main roof could be neglected under a determined filling ratio. The maximum tensile stress of the main roof in Panel 13080 was determined to be 6 MPa. From Figure 5, it could be concluded that the filling ratio of the gob should be greater than 82%, i.e., when $\varphi \geq 82\%$, the failure of the main roof is unlikely to occur.

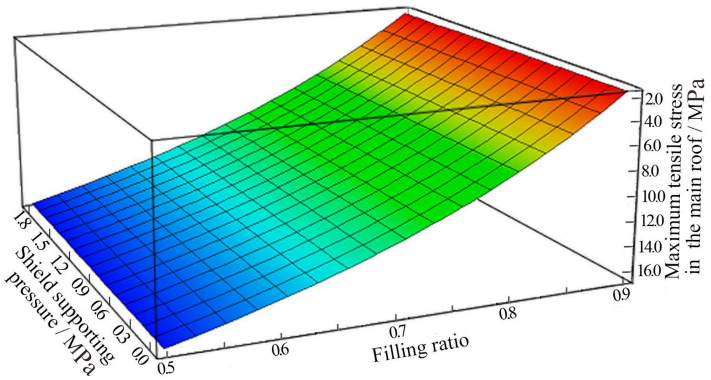

Figure 5. Relationship between the maximum tensile stress and the shield supporting pressure and filling ratio.

(2) Deflection of roof within the shield canopy length before backfilling

Since the deformation of the roof is not reversible, the deflection of the roof within the shield canopy length before backfilling is critical for the filling ratio. Based on the theory of the plate, the maximum deflection of the roof within the shield canopy could be observed at x = 8 m, y = 50 m, i.e., the middle of the panel and the end of the shield canopy.

To solve the maximum deflection, we substituted φ = 82%, E_1, E_3, F_1, F_3, x = 8 m and y = 50 m into Equation (23). The relationship between the maximum deflection $w_{\max}$ and the shield supporting pressure p was as follows:

$$w_{\max} = \frac{1}{0.82p \times 10^{-5}} + 5.87 \times 10^{-8}p - 0.119 \tag{29}$$

Based on Equation (29), the curve of the maximum deflection of main roof versus shield supporting pressure was drawn using the Maple software, as shown in Figure 6.

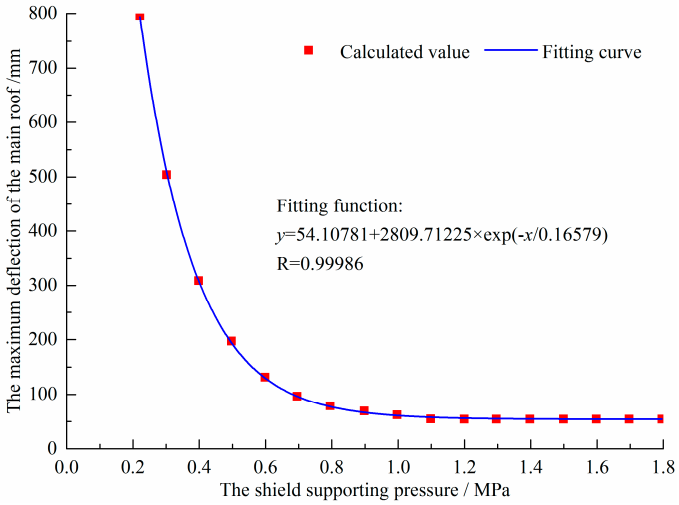

Figure 6. Relationship between the maximum deflection and the shield supporting pressure.

The following conclusions could be drawn based on Figure 6:

(1) When the filling ratio of the gob was constant, the relationship between the maximum deflection of the main roof within shield canopy length before backfilling, and the shield supporting pressure can be represented by a hyperbolic curve, which can be expressed by function $y = 54.10781 + 2809.71225 \times e^{-x/0.16579}$;

(2) The deflection of the main roof within the shield canopy length before backfilling decreases apparently with the increase of the shield supporting pressure. When the shield supporting pressure increases from 0.4 MPa to 0.9 MPa, the deflection of the main roof decreases by 77%, dropping from 350 mm to 80 mm, which would highly increase the backfilling height, and promote the filling ratio to a large extent. While the shield supporting pressure increases from 0.9 MPa to 1.8 MPa (implying high investment of shield), the decrease in roof deflection is relatively small, dropping from 80 mm to 54 mm, indicating a low increase of backfilling height and filling ratio. Based on this observation, it can be concluded that shield supporting pressure has a significant influence on the roof sagging within the shield canopy length, and adversely affect the filling ratio.

4. The Numerical Simulation of the Overburden Movement in CMCB

The previous results showed that the filling ratio φ and the shield supporting pressure p are the key factors influencing the movement of the roof in CMCB. And the filling ratio is the critical factor determining the fracture of the main roof. Therefore, this chapter demonstrated the movement characteristics of overburden with the filling ratios of 50%, 65%, 70%, 75%, 80%, 85%, 90%, employing numerical simulations.

4.1. Establishment of Numerical Model

The FLAC^{3D} numerical model is established based on the engineering geological conditions of Panel 13080 employed CMCB of Pingdingshan No. 12 Coal Mine, with a size of 550 m in length, 200 m in width, and 107 m in height, as shown in Figure 7.

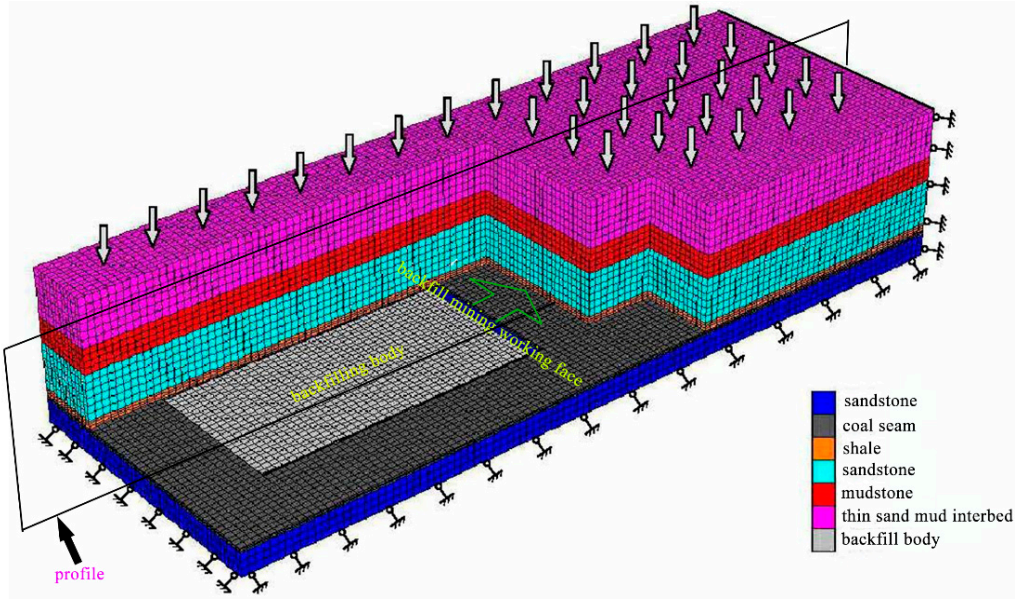

Figure 7. Numerical calculation model.

The width of the pillar is 100 m in strike direction, and 50 m in dip direction. The parameters of Panel 13080 and overburden were stated in 3.4. The model is divided into 264,000 units and 277,389 nodes. The upper boundary of the model is subjected to the uniform load of 6.5 MPa (the depth of cover upon thin sand mud interbed, H, was 267.9 m, and the average unit weight γ of the overburden was 24.5 kN/m^3), while surrounding boundary to the horizontal restrain, and the lower boundary to the vertical restrain. Two displacement measuring lines are set at the bottom of the immediate and the main roofs along the advancing direction of the panel, monitoring the sagging of the main and the immediate roofs respectively, during working face mining. Two stress measuring lines are set at the middle of the main roof and the middle of the backfill body along the advancing direction of the panel, monitoring abutment pressure and the internal pressure of the backfill body. The layout of the measuring lines are shown in Figure 8. The physical mechanical parameters of the coal and rock mass employed in the numerical model are shown in Table 1.

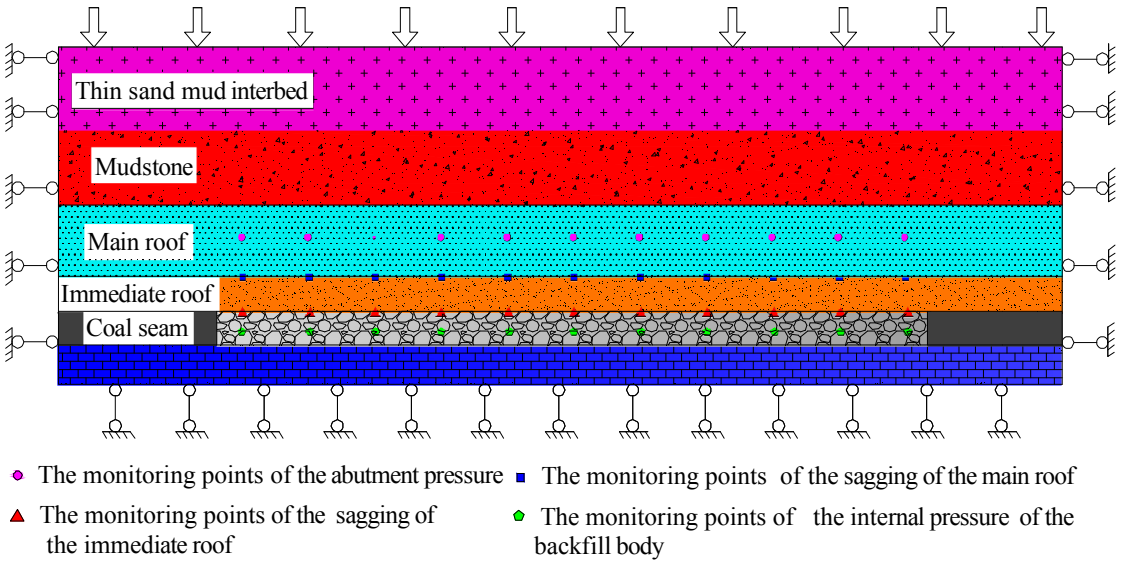

Figure 8. Monitoring points in the profile numerical model.

Table 1. Mechanical parameters of coal and rock strata.

Stratum	Thickness/m	Elastic Modulus/GPa	Poisson's Ratio	Tensile Strength/MPa	Cohesion/ MPa	Internal Friction Angle/°	Density/ kN·m^{-3}
thin sand mud interbed	33.6	23	0.27	2	6	31	24
mudstone layer	17.4	20	0.21	1.5	5	26	23.6
sandstone layer	31.5	28	0.25	2	7	28	26.3
shale layer	5.3	25	0.24	3.5	8	32	25.4
coal seam	3.3	3.5	0.33	0.1	1	25	14
sandstone layer	15.9	23	0.27	2	8	32	24

4.2. Simulation Results and Analysis

4.2.1. Roof Sagging Characteristics under Different Filling Ratios

The final monitoring data sets of the displacement were obtained after the stabile movement of the overburden. The final sagging curves of the immediate and the main roofs with different filling ratios versus the distance to the working face are shown in Figures 9 and 10. The maximum sagging of immediate roof and main roof versus different filling ratios are shown in Figure 11.

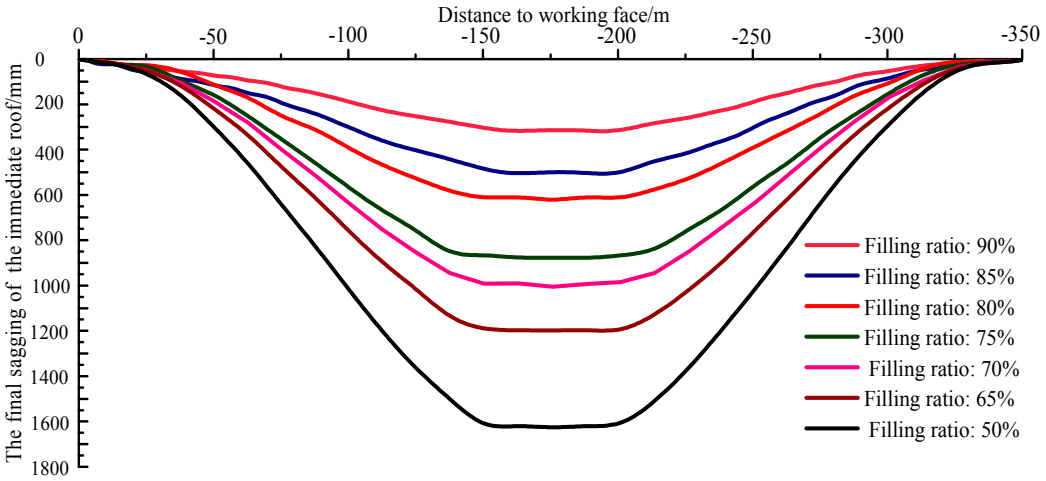

Figure 9. The final sagging curves of the immediate roof with different filling ratios.

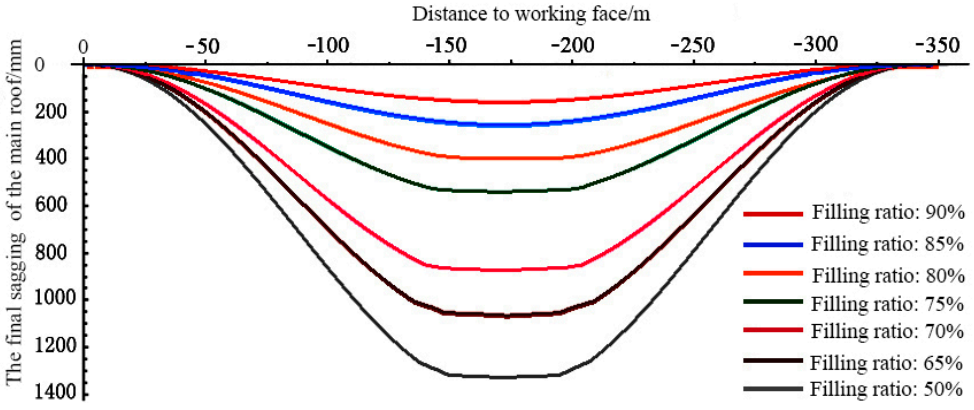

Figure 10. The final sagging curves of the main roof with different filling ratios.

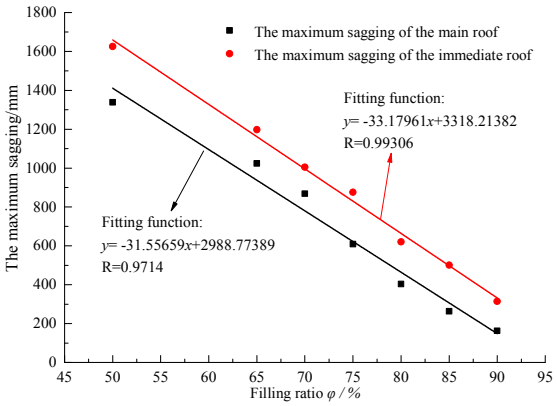

Figure 11. The maximum sagging of the immediate and the main roofs with the filling ratios.

(1) The final sagging curves of the immediate and main roofs are a bowl shaped along the advancing direction of panel. The maximum sagging of the immediate and main roofs both appeared in the middle of the gob, where the platform area appeared. The final sagging of the immediate and the main roofs gradually decreases from the middle of the gob to the ends and is close to zero at the position of the open-off cut and the stopping line.

(2) The maximum sagging of immediate roof decreases with the increase of the filling ratio of gob. When the filling ratio is 50%, 65%, 75%, 85%, 90%, the maximum sagging of immediate roof is 1625 mm, 1198 mm, 876 mm, 501 mm, 315 mm, respectively.

(3) The maximum sagging of main roof decreases with the increase of the filling ratio of the gob. When the filling ratio is 50%, 65%, 75%, 85%, 90%, the maximum sagging of main roof is 1338 mm, 1023 mm, 609 mm, 263 mm, 163 mm, respectively. When the filling ratio increased from 75% to 85%, the maximum sagging is severely decreased from 609 mm to 263 mm. It concludes that the main roof could remain continuously deformed without breaking when the filling ratio is above 85%, which is consistent with the elastic-thin-plate model.

4.2.2. Distributions of Abutment Pressure and Backfill Body Internal Pressure under Different Filling Ratios

(1) The distribution characteristics of abutment pressure

With the working face advancing a certain distance, the monitoring data of abutment pressure could be illustrated into a curve versus distance to the working face. The abutment pressure distributions under different filling ratios are shown in Figure 12.

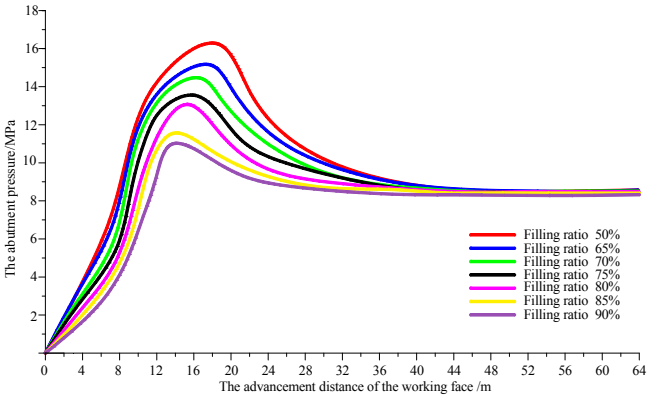

Figure 12. The abutment pressure distributions under different filling ratios with the advancement distance of the working face.

The following conclusions could be indicated based on Figure 12: under different filling ratios, the peak front of abutment pressure appears in the range of 10–20 m from the working face. When the filling ratio is 50%, the peak front value of the abutment pressure is 16 MPa with an influence range 25 m, while the filling ratio 85% with the peak front 11.5 MPa and an influence range 16 m. Thus, the filling ratio of gob has a significant influence on the value of abutment pressure and influence range, i.e., a higher the ratio results in a lower peak front and a smaller influence range. Additionally, when the filling ratio increases from 80% to 85%, the peak front and influence range decrease at a large extent, indicating that the main roof remains continuously deformed when the filling ratio is above 85%, without broken.

(2) The distribution characteristics of backfill body internal pressure

According to data from the stress measuring line set at the middle of the backfill body along the advance direction of the panel, the curves of the backfill body internal pressure under different ratios versus the working face advancing distance are illustrated in Figure 13. The stable periods of backfill body internal pressure under different ratios are shown in Figure 14.

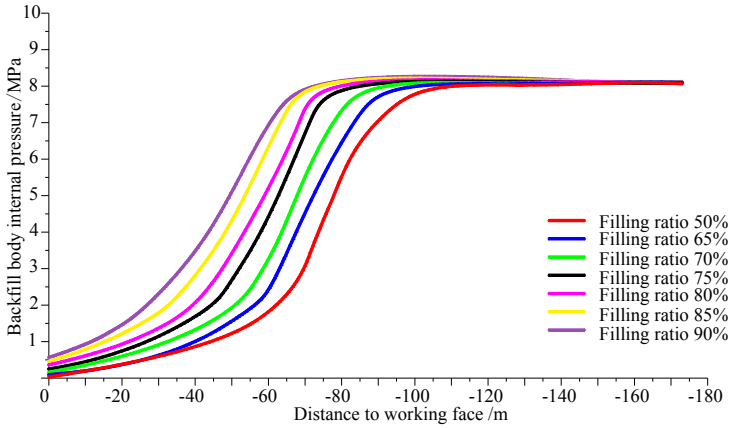

Figure 13. The distribution of backfill body internal pressure under different filling ratios.

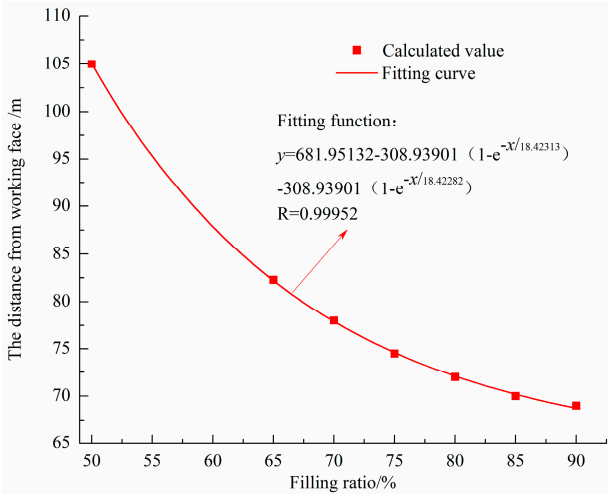

Figure 14. The distance from working face when backfill body internal pressure is stable under the condition of different filling ratios.

The following conclusions could be implied based on Figures 13 and 14:

(a) The backfill body internal pressure gradually increased with the increase of the advancing distance of the working face. The increase pressure curves could be divided into three phases, i.e., initial

pressure phase, accelerated increasing phase, and the stable pressure phase. In the initial pressure phase, the backfill body internal pressure slowly increases when the advancing distance of the working face increases, which indicates that the overburden subjected to the supports of front solid coal and rear backfill body bends slowly to the gob. Within the accelerated increasing phase, while the advancing distance of the face and span of the gob increase, the overburden accelerately sags to the gob, leading to the rapidly increase of the backfill body internal pressure. After the accelerated increasing phase, the internal pressure goes into a stable pressure phase, in which the internal pressure gradually approaches to the in-situ stress and the movement of the overburden reaches a new equilibrium.

(b) When the filling ratio is 50%, 65%, 70%, 75%, 80%, 85%, 90%, the advancing distance of the initial pressure phase is 68 m, 59 m, 52 m, 46 m, 43 m, 30 m, 20 m, respectively, and the advancing distance at which the internal pressure reaches stable is 105 m, 82 m, 78 m, 74 m, 72 m, 70 m, 69 m. Thus, the bigger the filling ratio is, the faster the backfill body internal pressure reaches stable period.

5. Engineering Test

5.1. Background

The underground layout of Panel 13080 employed CMCB of Pingdingshan No. 12 Coal Mine, and buildings location on or nearby the ground of the panel are shown in Figure 15. There are two villages and two mine surface plants located on or nearby the surface of Panel 13080. Donggaohuang Village lies on the west surface of Panel 13080, while Mifengwang Village lies on the east. Mine surface plant of No. 12 lies on the north surface of Panel 13080, while mine surface plant of Hezhuang Coal Mine lies on the south. The backfill material is from gangue dump of No. 12 Coal Mine. According to the former analysis, the designed filling ratio is 85%.

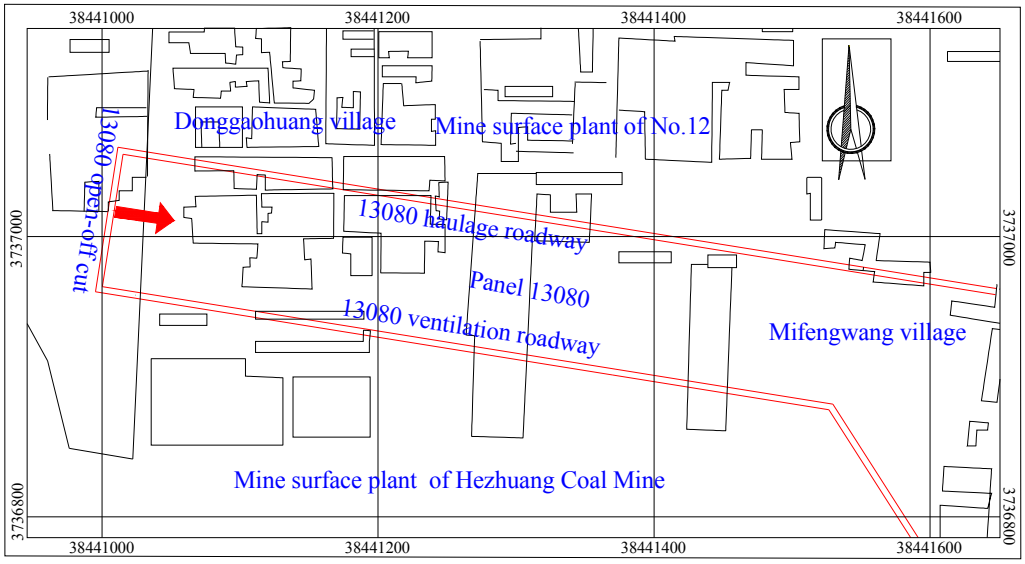

Figure 15. The surface-underground contrast layout of panel 13080.

5.2. Monitoring Layouts and Instruments

(1) Layout of roof sagging, pressure monitoring and instruments

With the advancement and backfilling of Panel 13080, the gob roof sagging, abutment pressure and backfill body internal pressure were monitored. The monitoring layouts are shown in Figure 16, and the monitoring instruments are shown in Figure 17, with parameters shown in Table 2. As shown

in Figure 16, #1 to #5 monitors for sagging of gob roof and #1 to #5 monitors for the backfill body internal pressure were installed when the working face advanced 20 m; #6 to #10 monitors for sagging of gob roof and #6 to #10 monitors for the backfill body internal pressure were installed when the working face advanced 40 m.

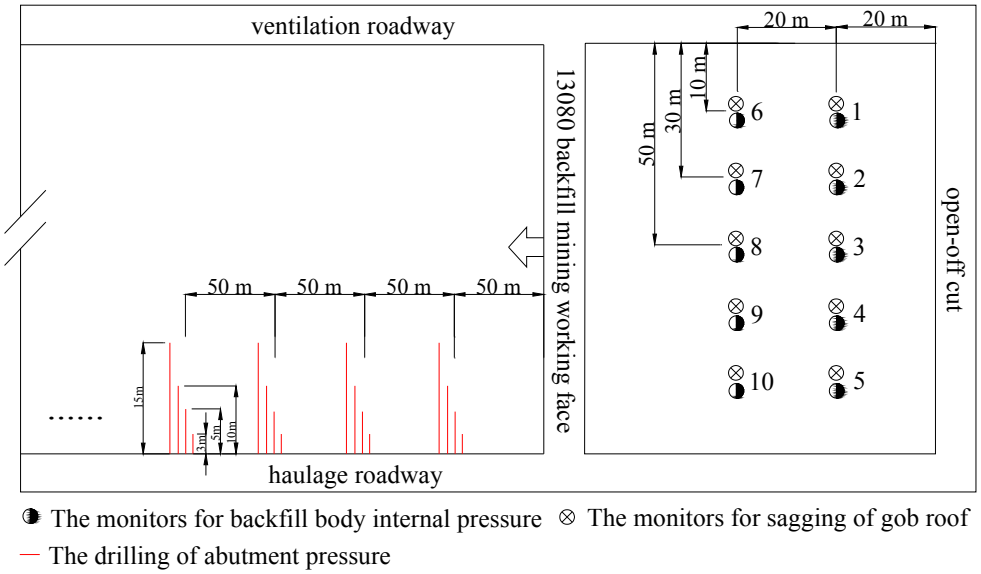

Figure 16. The monitoring layout of Panel 13080.

Figure 17. Mine pressure monitoring instruments. (**a**) Monitor for sagging of gob roof; (**b**) Monitor for backfill body internal pressure; (**c**) Borehole stress meter.

Table 2. Selection of mine pressure monitoring instruments.

Monitoring Items	Instruments	Model	Range
sagging of gob roof	Monitor for sagging of gob roof	GUD500	0–500 mm
backfill body internal pressure	Monitor for backfill body internal pressure	GPD30	0–30 MPa
abutment pressure	Borehole stress meter	GZY25	0–25 MPa (adapt to the borehole of 45–50 mm)

(2) Surface Sagging Monitoring Layout and instrument

According to the design principles of surface sagging observation [22], a surface sagging monitoring line was set along the dip direction of the panel, considering the distribution of the

buildings and roads. As shown in Figure 18, the surface sagging monitoring line was 1025 m, with 3 control observation (R_1, R_2, R_3, 50 m of interval) and 36 dynamic observation (25 m of interval). The robotic total station was employed in the surface sagging monitoring.

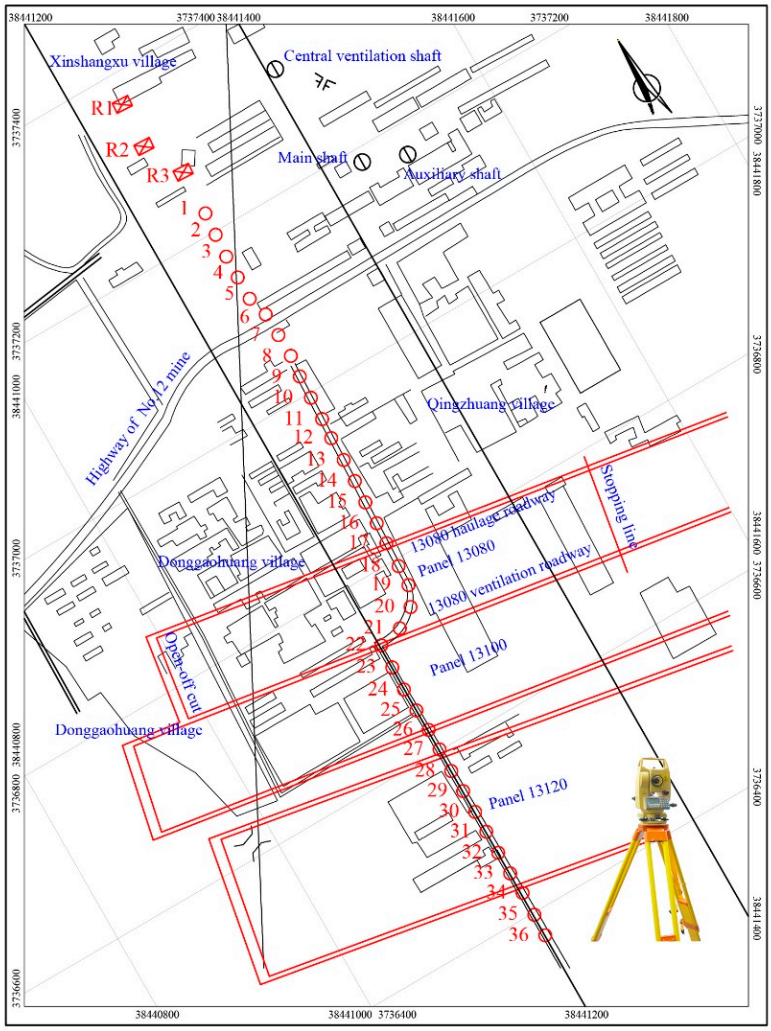

Figure 18. The sketch of the surface sagging observation line layout.

5.3. Monitoring Results and Analysis

(1) The sagging of the gob roof

Taken data collected from #3 roof sagging monitor (in the middle of the face line, 20 m away from the open-cut) and #8 roof sagging monitor (in the middle of the face line, 40 m away from the open-cut) for instance, the curves of the sagging of the gob roof versus advancement distance of the working face are as shown in Figure 19.

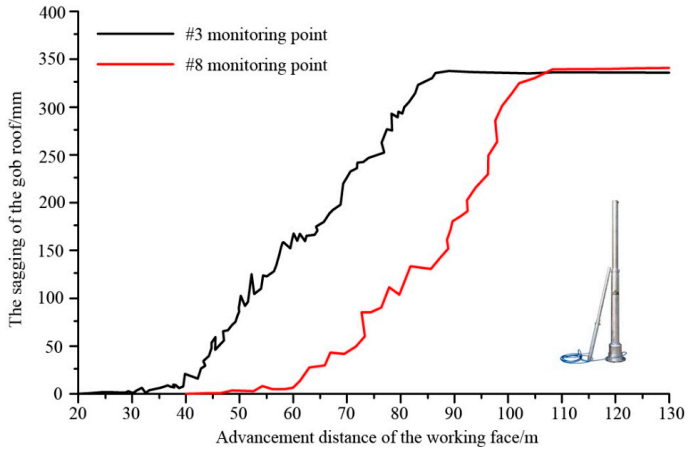

Figure 19. The sagging curves of the gob roof versus advancement distance of the working face.

The following conclusions could be drawn based on Figure 19:

(a) The curves of the gob roof sagging versus the working face advancement could be divided into three stages, i.e., the slowly sagging stage (0–20 m from the working face), the accelerated sagging stage (20–65 m from the working face) and the stable sagging stage (above 65 m from the working face), representing the three stages of the gob roof movement.

(b) In the slowly sagging stage (0–25 m from the working face), since the distance advancement of the working face was short, the pillar at the open-cut, solid coal subjected to the main load of the overburden, thus, the roof sagged slowly.

(c) With the distance advancement of the working face continue increasing, the gob roof acceleratedly sagged mainly bending as an intact stratum, corresponding to the accelerated sagging stage (20–65 m from the working face).

(d) After the face advancing 65 m, the sagging of the gob roof approximately verged to a stable stage. The backfill body mainly subjected to the overburden load. The maximum sagging of #3 and #8 were 340 mm, with the filling ratio of 89.5%, which was consistent with the theoretical results.

(2) Abutment pressure

The abutment pressure in different depth of solid coal was monitored by setting the borehole stress meters in front of working face, shown in Figure 20.

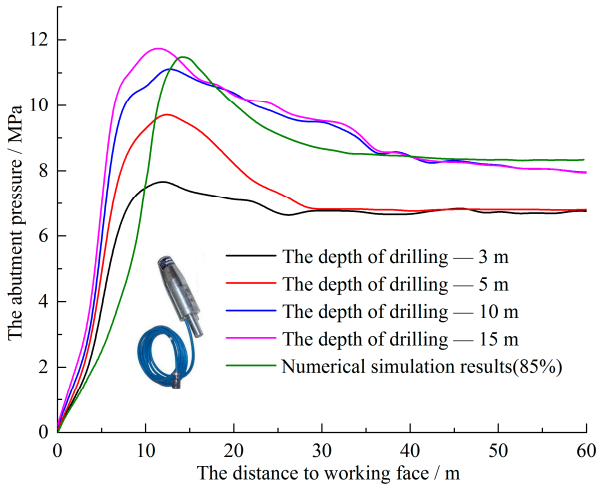

Figure 20. The abutment pressure in different depth of solid coal with the distance to working face.

The following conclusions could be drawn based on Figure 20:

(a) The abutment pressure distribution of CMCB panels is similar to the caving mining panels, with 4 zones along the advancement of the face, i.e., de-stress zone (0–5 m), stress rapid increase zone (5–15 m), stress decrease zone (15–25 m) and in-situ zone (after 25 m).

(b) However, the peak front and the influence range of the abutment pressures are gradually reduced compared to caving mining method. Furthermore, the maximum stress concentration factor is only 1.3, which is lower than the concentration factor in caving mining panels.

(c) When the drilling depth is 15 m, the monitoring results of abutment pressures are most close to the numerical simulation results. But the peak value of abutment pressures are slightly lower in numerical simulation, and the distance of peak position to the working face is large. It is considered that the numerical simulation cannot completely reproduce all the complicated mining geological conditions in engineering practice, but the error is still within the acceptable range.

(3) Backfill body internal pressure

Taken data collected from #3 pressure meter (in the middle of the face line, 20 m away from the open-cut) and #8 pressure meter (in the middle of the face line, 40 m away from the open-cut) for instance, the curves of the backfill body internal pressure versus advancement distance of the working face are shown in Figure 21.

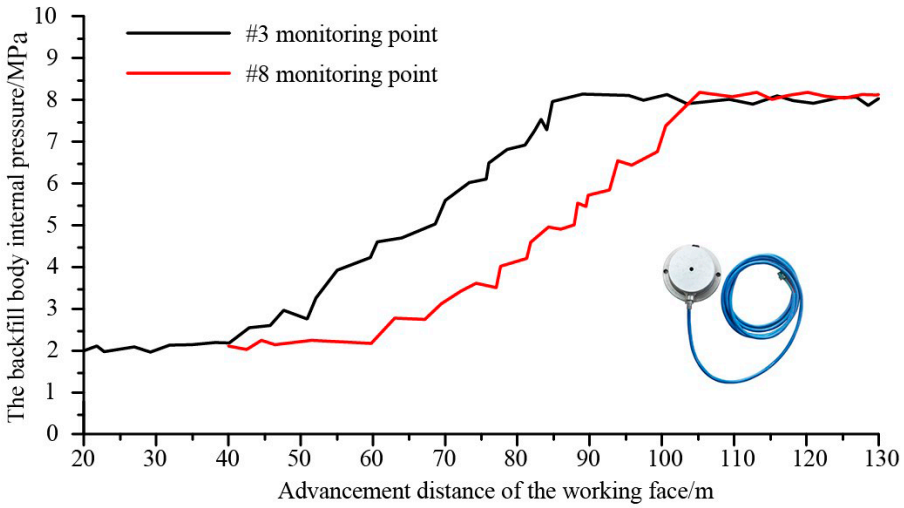

Figure 21. The curves of backfill body internal pressure of monitoring points #3 and #8.

The following conclusions could be drawn based on Figure 21:

(a) The backfill body internal pressure curves versus the advancement distance of the working face could be divided into three stages: the initial stress stage (0–20 m from the working face), the stress rapidly increasing stage (20–65 m from the working face) and the stress stability stage (after 65 m from the working face), in correlation with the three stages of gob roof sagging, i.e., the slowly sagging stage, the accelerated sagging stage and the stable sagging stage.

(b) In initial stress stage, the backfill body internal pressure varied from 1.8 MPa to 2.5 MPa, while in the stress rapidly increasing stage, it increase rapidly from 2.5 MPa to approximate 8.5 MPa. It indicated that the main carriers of the overburden load changed from the solid coal of the face and the open-cut pillars in the initial stage to backfill body in the stress rapidly increasing stage.

(c) After 65 m, the backfill body internal pressure was gradually stabilized with the distance advancement of the working face, with a maximum value of approximate 8.6 MPa which is close to the in-situ stress. It shows that the movement of the overburden at this stage was close to stable under the support of the backfill body.

(4) Measurement of surface sagging

The curves of maximum surface sagging from the data through field measurement and prediction software MSPS [29] with a filling ratio of 0%, 85% were illustrated, as shown in Figure 22 and Table 3.

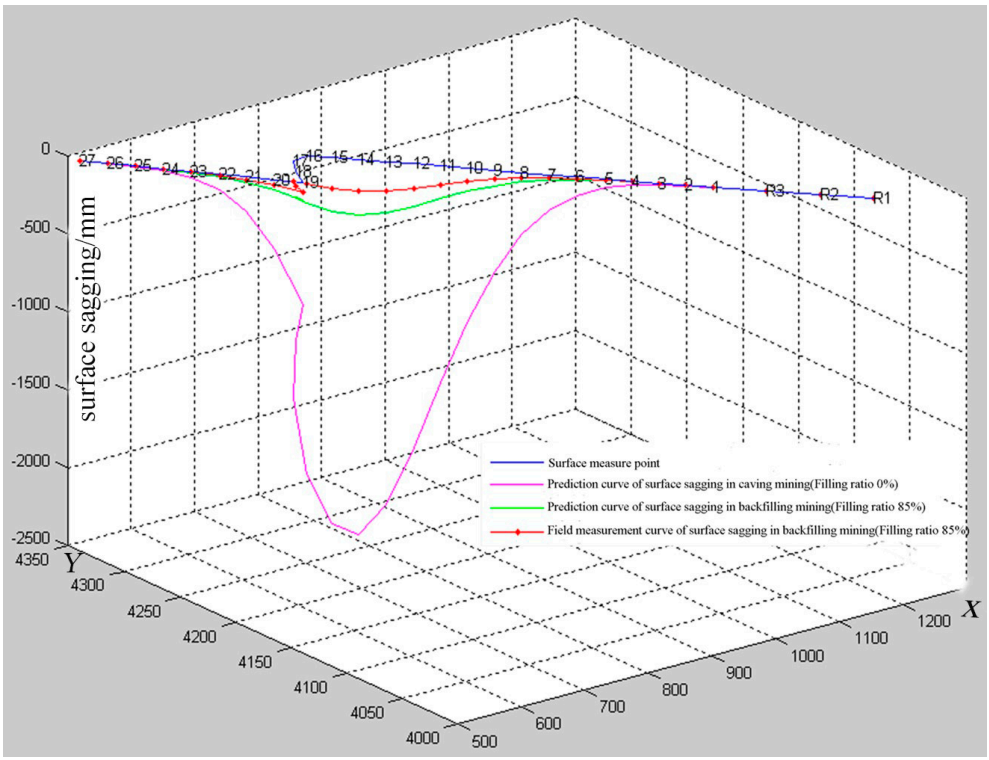

Figure 22. Surface sagging predicted and field measurement curves of Panel 13080.

As show in Figure 22 and Table 3, after the mined-out of Panel 13080, the maximum value of surface sagging was 173 mm, and the maximum horizontal deformation is 0.2 mm/m. According to the Building, Railway and Water bodies Pillars Remain and Mining Act of 2000, damage level of the buildings on the ground is I level (very slightly) without the need for reinforcement or repair, and it's in consistent with the theoretical results.

Table 3. Data of surface movement prediction and field measurement of Panel 13080.

Compared Items	Prediction		Field Measurement
Filling ratio	0%	85%	92.2%
Equivalent mining height/mm	3300	580	340
Maximum sagging/mm	2040	220	173
Maximum horizontal deformation/mm	9.5	0.66	0.2
Damage level of building	III level, ponding	I level (very slight)	I level (very slight)

6. Conclusions

(1) The elastic-thin-plate mechanical model for overburden in coal mining with compacted backfilling (CMCB) was established according to the deformation characteristics of the surrounding rocks. The deflection equation, bending moment equation, and maximum tensile stress equations

associated with the main roof in CMCB were derived from virtual displacement principle. The critical conditions of main roof failure were also obtained.

(2) By theoretical analysis, the main roof stability is primarily controlled by the filling ratio φ and is non-correlated to the shield supporting pressure p. The relationship between the maximum sagging of main roof within the shield canopy and shield supporting pressure was given, which shows that the support pressure has a significant control effect on the sagging of the roof within the shield canopy length, and adversely affects the filling ratio.

(3) The numerical simulation results show that the maximum sagging of immediate roof and main roof decreases with the increase of the filling ratios of gob. When the filling ratio increased from 75% to 85%, the maximum sagging is decreased from 609 mm to 263 mm, respectively. With the increase of the filling ratio of gob, the peak value and the influence range of the abutment pressure are gradually reduced, and the stability period of backfill body internal pressure is shortened gradually.

(4) Filling ratio of working face was determined to be 85% according to the theoretical analysis and the numerical calculation results. The abutment pressure, the sagging of roof, the backfill body internal pressure, surface sagging were monitored and analysed. Monitoring results show that the measured data are consistent with the theoretical analysis and numerical simulation results.

Acknowledgments: Financial support for this work provided by the Fundamental Research Funds for the Central Universities (2015XKMS001), Qing Lan Project of JiangSu Province, National Key Basic Research Program of China (2013CB227905) and Top-notch Academic Programs Project of Jiangsu Higher Education Institutions are gratefully acknowledged.

Author Contributions: Yanli Huang proposed the innovative points and conceived; Junmeng Li established and solved the mechanical model; Tianqi Song and Guoqiang Kong analyzed the data; Junmeng Li and Guoqiang Kong monitored the engineering test results; Tianqi Song and Meng Li performed the simulation; Yanli Huang and Junmeng Li wrote the paper; Junmeng Li and Meng Li revised the paper.

Conflicts of Interest: The authors declare no conflict of interest.

References

1. Morteza, S. A review of underground mine backfilling methods with emphasis on cemented paste backfill. *Electron. J. Geotech. Eng.* **2015**, *20*, 5182–5208.
2. Yao, Y.; Cui, Z.; Wu, R. Development and challenges on mining backfill technology. *J. Mater. Sci. Res.* **2012**, *1*, 73–78. [CrossRef]
3. Potvin, Y.; Thomas, E. *Handbook on Mine Fill*; Australian Centre for Geomechanics: Crawley, Australia, 2005.
4. Pokharel, M.; Fall, M. Combined influence of sulphate and temperature on the saturated hydraulic conductivity of hardened cemented paste backfill. *Cem. Concr. Compos.* **2013**, *38*, 21–28. [CrossRef]
5. Ghirian, A.; Fall, M. Coupled thermo-hydro-mechanical–chemical behaviour of cemented paste backfill in column experiments: Part II: Mechanical, chemical and microstructural processes and characteristics. *Eng. Geol.* **2014**, *170*, 11–23. [CrossRef]
6. Yao, Y.; Sun, H. A novel silica alumina-based backfill material composed of coal refuse and fly ash. *J. Hazard. Mater.* **2012**, *213*, 71–82. [CrossRef] [PubMed]
7. Miao, X.X.; Zhang, J.X.; Guo, G.L. Study on waste-filling method and technology in fully-mechanized coal mining. *J. China Univ. Min. Technol.* **2010**, *35*, 1–6.
8. Zhang, J.X.; Miao, X.X.; Guo, G.L. Development status of backfilling technology using raw waste in coal mining. *J. Min. Saf. Eng.* **2009**, *26*, 395–401.
9. Al Heib, M.M.; Didier, C.; Masrouri, F. Improving short- and long-term stability of underground gypsum mine using partial and total backfill. *Rock Mech. Rock Eng.* **2010**, *43*, 447–461. [CrossRef]
10. Zhang, J.; Zhang, Q.; Huang, Y.; Liu, J.; Zhou, N.; Zan, D. Strata movement controlling effect of waste and fly ash backfillings in fully mechanized coal mining with backfilling face. *Min. Sci. Technol.* **2011**, *21*, 721–726. [CrossRef]
11. Huang, Y.L.; Zhang, J.X.; Zhang, Q.; Nie, S.J.; An, B.F. Strata movement control due to bulk factor of backfilling body in fully mechanized backfilling mining face. *J. Min. Saf. Eng.* **2012**, *29*, 162–167.

12. Bock, S.; Prusek, S. Numerical study of pressure on dams in a backfilled mining shaft based on PFC^{3D} code. *Comput. Geotech.* **2015**, *66*, 230–244. [CrossRef]
13. Yu, B.; Zhang, Z.Y.; Kuang, T.J. Stress changes and deformation monitoring of longwall coal pillars located in weak ground. *Rock Mech. Rock Eng.* **2016**, *49*, 3293–3305. [CrossRef]
14. Zhang, J.X.; Li, J.; An, T.L.; Huang, Y.L. Deformation characteristic of key stratum overburden by raw waste backfilling with fully-mechanized coal minning technology. *J. China Coal Soc.* **2010**, *35*, 357–362.
15. Chen, J.; Du, J.P.; Zhang, W.S.; Zhang, J.X. An elastic model of overlying strata movement during coal mining with gangue back-filling. *J. China Univ. Min. Technol.* **2012**, *41*, 14–19.
16. Zhou, Y.J.; Chen, Y.; Zhang, J.X.; He, Q. Control principle and technology of final compression ratio of backfilling materials. *J. Min. Saf. Eng.* **2012**, *29*, 351–356.
17. Qian, M.G. *Mining Pressure and Strata Control*; China University of Mining and Technology Press: Xuzhou, China, 2003.
18. Guo, G.L.; Zhu, X.J.; Zha, J.F.; Qiang, W.A. Subsidence prediction method based on equivalent mining height theory for solid backfilling mining. *Trans. Nonferrous Met. Soc. China* **2014**, *24*, 3302–3308. [CrossRef]
19. Seryakov, V.M. Mathematical modeling of stress-strain state in rock mass during mining with backfill. *J. Min. Sci.* **2014**, *50*, 847–854. [CrossRef]
20. Li, S.Q.; Zheng, G. Analytic solution of beams on Winkler foundation under complex conditions. *Chin. J. Geotech. Eng.* **2008**, *30*, 873–879.
21. Wu, L.Y. *Theory of Plate and Shell*; Shanghai Jiaotong University Press: Shanghai, China, 1989.
22. Al-Tholaia, M.M.; Al-Gahtani, H.J. RBF-based meshless method for large deflection of elastic thin plates on nonlinear foundations. *Eng. Anal. Bound. Elem.* **2015**, *51*, 146–155. [CrossRef]
23. Li, L. Analytical solution for determining the required strength of a side-exposed mine backfill containing a plug. *Can. Geotech. J.* **2014**, *51*, 508–519. [CrossRef]
24. Sargsyan, A.H.; Sargsyan, S.H. Dynamic model of micropolar elastic thin plates with independent fields of displacements and rotations. *J. Sound Vib.* **2014**, *333*, 4354–4375. [CrossRef]
25. Xu, Z. *Elasticity*; Higher Education Press: Beijing, China, 1990.
26. Liu, J.H. Elastic-thin-plate bending method for evaluating reducing-subsidence effectiveness by injecting grout into separated strata in coal mine. *Eng. Mech.* **2009**, *26*, 252–256.
27. Qian, M.G.; Miao, X.X.; Xu, J.L. *The Theory of Key Strata in Ground Control*; China University of Mining and Technology Press: Xuzhou, China, 2003.
28. Peng, S.S. *Coal Mine Ground Control*; John Wiley & Sons Inc.: Hoboken, NJ, USA, 1978.
29. Miao, X.X.; Huang, Y.L.; Ju, F.; Mao, X.B.; Guo, G.L.; Zhang, J.X. Strata movement theory of dense backfill mining. *J. China Univ. Min. Technol.* **2012**, *41*, 863–867.